Direct Estimation of Cardiac Biventricular Volumes With an Adapted Bayesian Formulation

Zhijie Wang*, Mohamed Ben Salah, Bin Gu, Ali Islam, Aashish Goela, and Shuo Li

***Abstract*—Accurate estimation of the ventricular volumes is essential to the assessment of global cardiac functions. The existing estimation methods are mostly restricted to the left ventricle (LV), and often require segmentation which is challenging and computationally expensive. This paper proposes to estimate the volumes of both LV and right ventricle (RV) jointly with an efficient *segmentation-free* method. The proposed method employs an adapted Bayesian formulation. It introduces a novel likelihood function to exploit multiple appearance features, and a novel prior probability model to incorporate the area correlation between LV and RV cavities. The method is validated on a comprehensive dataset containing 56 clinical subjects (3360 images in total). The experimental results demonstrate that the estimated biventricular volumes are highly correlated to their independent ground truth. As a result, the proposed method enables a direct, efficient, and accurate assessment of global cardiac functions.**

***Index Terms*—Bayesian estimation, cardiac function assessment, cardiac MRI, ventricular volume.**

I. Introduction

CARDIOVASCULAR diseases are the leading cause of death in western countries [1]. Diagnosis and treatment of these diseases usually require the assessment of cardiac functions for both left ventricle (LV) and right ventricle (RV). Many of those functions can be quantified using ventricular volumes, such as ejection fraction (EF) and stroke volume. Since estimating ventricular volumes through manual segmentation is extremely slow and tedious, many automatic methods have been proposed. However, accurate estimation of ventricular volumes is still challenging for LV and remains completely unsolved for RV [2]. In the following, we give a brief review on the existing ventricular analysis methods, most of which apply only to LV and rely on computationally expensive segmentation techniques. Traditional methods such as thresholding, region growing, edge detection, and clustering [3], [4] are typically based on low-level image information. These methods fail dramatically when the neighboring structures to the ventricles present similar photometric profiles such as the fat which often has a bright appearance [5]. Other popular yet more recent methods are the variational approaches based on energy minimization such as graph cuts, active contours/level sets, and registration [6]–[8]. They are well known to be sensitive to initialization, ad-hoc parameters, and require a heavy computational load. Moreover, techniques like active appearance and shape models [9], [10] are either limited to mid-ventricular, end-diastolic images [2] or treat the two ventricles independently. A recently published comprehensive review which points to the challenges of cardiac image segmentation can be found in [2]. The most closely related work to our method is the recent study of Afshin *et al.* [11], which computes the cavity area of the LV from image statistics (Bhattacharyya similarity between image distributions) and simple user inputs (two boxes, one inside the LV cavity and one enclosing the cavity) via machine learning and without any segmentation step. However, this method is restricted to the LV, could not be straightforwardly extended to the RV, and is very sensitive to the user inputs [12]. In fact, it assumes a strong correlation between the considered statistics and the LV cavity areas as shown in Fig. 1(d) and (e). Contrarily, the statistics within the RV region of interest (ROI) do not correlate well with the RV cavity areas as shown in Fig. 1(i) and (j). This is because in the RV ROI, undesirable structures with similar intensity profile to the cavity may appear [as shown in Fig. 1(g)] and inseparably contribute to the considered statistics alone with the cavity. Therefore, the method in [11] is not applicable to the RV.

In this paper, we propose a novel method to estimate the biventricular volumes jointly without the need for segmentation. As shown in Fig. 2(a) and (b), a minimal user interaction is required in the form of two landmarks placed on each slice in the first frame of the MRI sequence. The biventricular volumes throughout the cardiac cycle are then automatically estimated in real time. Consequently, cardiac functions can be assessed accurately and efficiently. This study is of significant clinical importance, and its clinical validation has been accepted in Radiological Society of North America (RSNA) 2013 [13] as an abstract. In summary, three major contributions exist in this study:

1) a novel approach for estimating both LV and RV volumes jointly and without segmentation;

Manuscript received July 24, 2013; revised October 24, 2013 and December 17, 2013; accepted January 7, 2014. Date of publication January 9, 2014; date of current version March 17, 2014. *Asterisk indicates corresponding author.*

*Z. Wang is with the Department of Medical Biophysics, University of Western Ontario, London ON N6A 3K7, Canada (e-mail: zhijie@ualberta.ca).

M. B. Salah is with the Department of Computing Science, University of Alberta, Alberta AB T6G 2R3, Canada (e-mail: mbensala@ualberta.ca).

B. Gu are with the Department of Medical Biophysics, University of Western Ontario, London ON N6A 3K7, Canada (e-mail: bin.gu@uwo.ca).

A. Islam is with Medical Imaging, University of Western Ontario, Ontario, ON N6A 3K7, Canada, and also with the Radiology, Saint Joseph's Health Care, London, Ontario, ON M6R 1B5, Canada (e-mail: ali.islam@sjhc.london.on.ca).

A. Goela is with the Medical Imaging, University of Western Ontario, Ontario, ON N6A 3K7, Canada, and also with Radiology, London Health Sciences Center, London, Ontario, ON N6G 2V4, Canada (e-mail: Aashish.Goela@lhsc.on.ca).

S. Li is with the GE Health Care, London, Ontario, Canada, and also with the Department of Medical Biophysics, University of Western Ontario, Ontario, ON N6A 3K7, Canada (e-mail: Shuo.Li@ge.com).

Color versions of one or more of the figures in this paper are available online at http://ieeexplore.ieee.org.

Digital Object Identifier 10.1109/TBME.2014.2299433

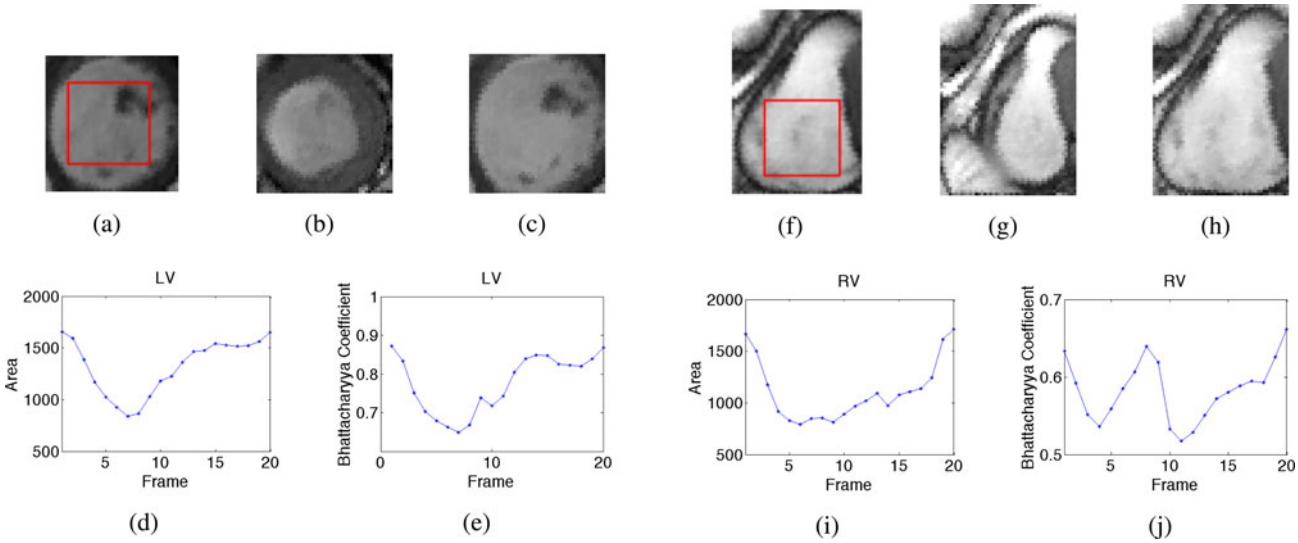

Fig. 1. Comparison between LV and RV illustrates that the method in [11] does not apply to RV. (a) Reference image of LV (inside red square); (b) end-systolic frame of LV; (c) end-diastolic frame of LV; (d) and (e) LV cavity areas correlate well with the Bhattacharyya statistics over the cardiac cycle; (f)–(h) reference image, end-systolic, and end-diastolic frames of RV; (i) and (j) RV cavity areas do not correlate with the Bhattacharyya statistics.

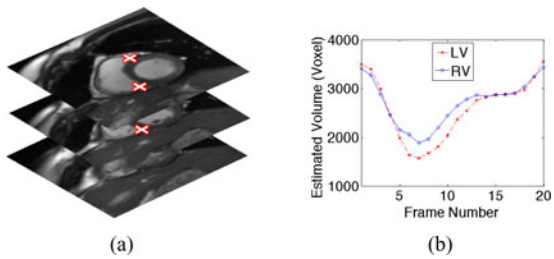

Fig. 2. (a) User selected landmarks; (b) estimated volumes of LV and RV over the cardiac cycle.

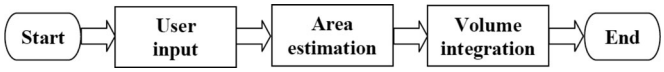

Fig. 3. Flow chart of estimating the biventricular volumes.

2) a novel likelihood function making use of multiple appearance features; and
3) a novel prior probability model exploiting area correlation information.

The remainder of this paper is organized as follows. In Section II, the overview of the proposed volume estimation method will be described. Then, the key component of the method, cavity area estimation, will be detailed in Section III. Section IV includes the experimental results that illustrate the performance of the proposed method, and finally, a conclusion is drawn in Section V.

II. Method Overview

This section gives an overview of the proposed method for estimating the biventricular volumes in a short-axis view MRI sequence. As explained by the flow chart in Fig. 3, the proposed method consists of three consecutive steps: 1) a minimum user input is conducted for ROI extraction, 2) the cavity areas of LV and RV in each slice and each frame are estimated automatically, and 3) the volumes of both LV and RV are obtained by integrating the corresponding cavity areas along the sagittal direction. The first and third steps will be introduced in the following, while the second step (area estimation) will be explained in more details in the next section.

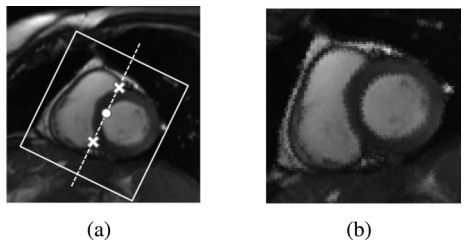

Fig. 4. (a) ROI construction where the user selected landmarks are shown by the two white crosses; (b) ROI extracted from (a).

A. User Input

As shown in Fig. 4(a), we select a single ROI that encloses both the LV and the RV. The selection requires a minimal user intervention in the form of two landmarks [depicted by the two white crosses in Fig. 4(a)] placed on each slice of the short-axis view MRI in the first frame. The selected landmarks are anatomically significant in order to keep a certain consistency between different potential ROIs. As depicted in Fig. 4(a), we use the two attachment points of the right-ventricular wall to the left-ventricular septal wall as anatomical landmarks. The ROI [specified by the white rectangle in Fig. 4(a)] is then computed automatically as follows. The central point of the two landmarks [white dot in Fig. 4(a)] is the center of the squared ROI whose scale is twice as large as the distance between the landmarks. The orientation of the ROI is determined by the central line [dashed line in Fig. 4(a)] linking the two landmarks. Finally, the image within the selected ROI is clipped, rotated so that the central line becomes vertical and separates between the LV on

its right side and the RV on its left side, then rescaled (to 40×40 pixels in this study) as depicted by Fig. 4(b).

Although simple to proceed, the ROI selection procedure described previously brings the following advantages: 1) as mentioned previously, only a single ROI is required for both LV and RV rather than two individual ones; 2) the LV and the RV are jointly examined within the selected ROI by exploiting their correlation information in the prior probability model proposed in subsection III-C; and 3) using landmarks with anatomical significance makes the ROI selection consistent, so that the final estimated results are robust to intra- and interuser variability as demonstrated in the experimental section.

B. Volume Integration

In the proposed method, the ventricular volumes of LV and RV are approximated by integrating the cavity areas in short-axis view slices along the sagittal direction. Specifically, the overall volume V is obtained by summing the volume of each slice which is computed as the product of the corresponding cavity area A_i and the slice thickness h,

$$V = \sum_i A_i \cdot h. \tag{1}$$

In the previous equation, the key component is to estimate the cavity area A_i, which comprises our main contribution in this paper. This problem is formulated and tackled (different from most of the related works) using an adapted Bayesian formulation. Details are presented in the following section.

III. Bayesian Estimation of Cavity Area

This section formulates the problem of estimating a cavity area, given an input image, in the Bayesian framework. The Bayesian framework has the following two advantages among others which are appealing to our problem. It is efficient and often leads to global optima compared to active contour/level set and registration methods. It is also very convenient for incorporating a variety of models/constraints related to appearance, motion, etc. In the following, we will first present the problem formulation, and then propose a likelihood function and a prior probability model within the Bayesian framework. Finally, we will detail the implementation.

A. Problem Formulation

General Bayesian Formulation: In the Bayesian framework, statistical pattern recognition problems amount to estimating the posterior probability density of an object parameterized by X given its prior $p(X)$ and the observation Z. Generally, the posterior probability of X given the observation Z is written as follows:

$$p(X|Z) \propto p(Z|X)p(X) \tag{2}$$

where $p(Z|X)$ is the likelihood function modeling the probability of observing Z given the object state X, and $p(X)$ is the prior probability of the object state.

Adapted Bayesian Formulation: As shown in Fig. 5, our objects of interest, LV and RV, are two individual heart chambers

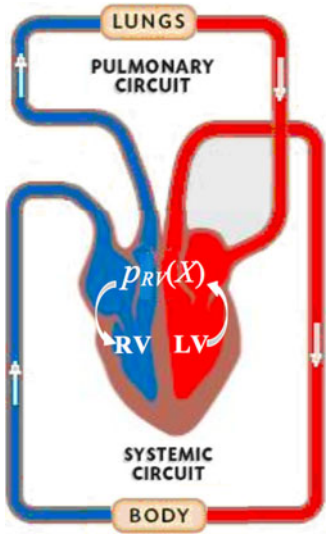

Fig. 5. LV and RV belong to a closed circulation system. Therefore, LV can provide a prior [$p_{\mathrm{RV}}(X)$] to RV based on their correlation.

belonging to a closed circulation system. Due to their connection in both physical and logical aspects, the two ventricles share the same motion pattern, cyclically expanding (during a diastolic period) and contracting (during a systolic period). As a consequence, the volume variations of the two ventricles essentially resemble each other in their patterns as shown in Fig. 2(b). This relationship can be approximated by a linear correlation model which indicates two variables that increase or decrease proportionately (not necessarily equivalently) to each other. The same relationship reflects in a short-axis view slice too. In other words, the two cavity areas of LV and RV are linearly correlated too because they increase and decrease proportionally due to the two cavities' synchronized motion. Note that the increment and decrement of the two cavity areas are proportional but not equivalent. In fact, the variation degree of the RV short-axis cavity area is smaller than LV, since RV has a predominantly longitudinal shortening effect [14]. However, this difference between the variation degrees does not affect our assumed linear correlation, because the assumption only requires the two cavity areas to change proportionately rather than equivalently. Therefore, between LV and RV's short-axis areas there is essentially a linear correlation model which will be validated and exploited in this paper. Driven by this model, we adapt the general Bayesian formulation to our specific biventricle estimation problem. The adapted formulation is designed as follows:

$$p(X|Z) = \begin{cases} p_{_{LV}}(X|Z) \propto p(Z|X)p_{_{LV}}(X) \\ p_{_{RV}}(X|Z) \propto p(Z|X)p_{_{RV}}(X). \end{cases} \tag{3}$$

Two corresponding Bayesian models are proposed for LV and RV, while their connections are handled by $p_{\mathrm{RV}}(X)$ (RV's prior probability model) which is modeled as a function of $p_{\mathrm{LV}}(X|Z)$ (LV's posterior probability). Specifically, $p_{\mathrm{RV}}(X)$ exploits the estimated LV areas as a prior based on the correlation between LV and RV. Here, LV is chosen to provide a strong prior for RV estimation, a common challenge for many existing methods,

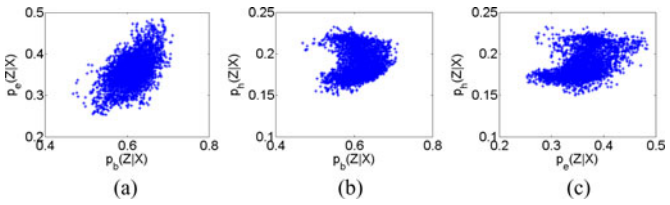

Fig. 6. Study of the independency between the three proposed appearance models. Only weak correlations are shown between the three models computed from an input image and its 3300 hypothesized labelings.

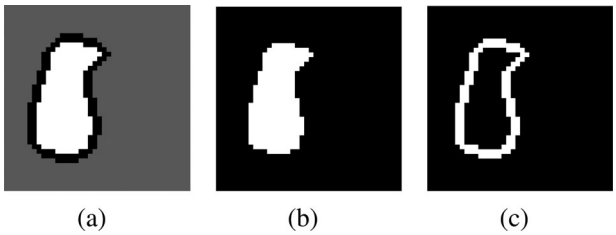

Fig. 7. Example masks used in the three proposed appearance models (taking the RV case as example). (a) Blob mask used to capture the blob feature by computing its dot product with the input image; (b) homogeneity mask used to specify the cavity region within which the homogeneity is computed; (c) edge mask used to capture the edge feature by computing its dot product with an edge image.

because LV's estimation can be accurate and reliable due to its circular geometry in short-axis view.

Direct Area Estimation: Based on the adapted Bayesian formulation in (3), the object state is defined as $X = [X_1, \ldots, X_Q]$ where $X_q \in \{0, 1\}$ is the label assigned to the qth pixel in the input image and $q \in \{1, \ldots, Q\}$. The two labels $\{0, 1\}$ correspond to "background" and "LV/RV." Clearly, object state X is a labeling of the image, and it partitions the image into two segments: cavity and background. Our method is fundamentally different from the existing segmentation-based methods which obtain the solution X in a generative way, i.e., they directly search for the optimal segmentation using various approaches, for instance thresholding, graph cut, level set, etc. The cavity area is then computed systematically from the obtained segmentation. Differently, our method computes the cavity area in an inference way, i.e., it first estimates the posterior probability of the object state X using the Bayesian inference method, and then computes the cavity area as the expectation of a function of X. Specifically, once the posterior probability $p(X|Z)$ is estimated, the mean cavity area of LV/RV is computed as a function of the posterior:

$$\mathcal{E}[A(X)|Z] = \sum_{X \in \{0,1\}^Q} A(X) p(X|Z) \tag{4}$$

where

$$A(X) = \textstyle\sum_q \delta(X_q, 1) \tag{5}$$

with $\delta(a, b)$ as the Kronecker delta function. $A(X)$ computes the LV/RV cavity area in X by counting the pixels labeled as 1.

Till now, the formulation of estimating a cavity area has been presented. In the following, we focus on the two major contributions embedded within the two essential components of our adapted Bayesian formulation: a novel multifeature likelihood function [$p(Z|X)$ in (3)] and a novel area correlation prior probability model [$p_{\mathrm{RV}}(X)$ in (3)].

B. Proposed Likelihood Function

We propose to compute the likelihood function $p(Z|X)$ using three features: blob, homogeneity, and edge in this form:

$$p(Z|X) = p_b(Z|X) p_h(Z|X)^{\alpha} p_e(Z|X)^{\beta} \tag{6}$$

where $p_b(Z|X)$, $p_h(Z|X)$, and $p_e(Z|X)$ are respectively blob, homogeneity, and edge feature-based appearance models that we detail in the following. The parameters α and β adjust the relative importance of each of the three models. Here, the three models are assumed to be conditionally independent to each other given the object state X, which is a widely used assumption for integrating multiple features/models [15]. This is supported by the following study in our dataset. Given an input image and 3300 hypothesized object states collected from manual segmentation of our dataset, the three models $p_b(Z|X)$, $p_h(Z|X)$, and $p_e(Z|X)$ are computed and plotted against each other in Fig. 6. A low degree of correlation is shown between the blob and edge-based appearance models, while the others show even weaker correlations.

1) Blob Feature-Based Appearance Model: Blob feature [16] is particularly useful in medical imaging where objects can have a blob-like appearance, i.e., the inside area is brighter or darker than its surrounding area. In our problem, the LV/RV cavity is typically brighter than the neighboring structures in MRI, which makes blob feature an appropriate tool for extracting cavity regions. Therefore, we propose an appearance model based on the blob feature,

$$\begin{aligned} p_b(Z|X) &= (1 + \langle Z, f^b(X) \rangle)/2 \\ &= (1 + \sum_{q \in \{1,\ldots,Q\}} Z_q f^b_q(X))/2 \end{aligned} \tag{7}$$

where $f^b(X)$ is an adaptive mask [as the example shown in Fig. 7(a)] constructed based on the object state X, and $f^b_q(X)$ is the qth pixel in the mask. This mask is composed of the cavity region [the white region in Fig. 7(a)], the narrow band region [the black region in Fig. 7(a)], and the remaining pixels [shown in gray in Fig. 7(a)]. The pixel weights corresponding to the three regions sum to 1, -1, and 0 respectively. The dot product between the input image and the adaptive mask, $\langle Z, f^b(X) \rangle$, naturally captures the image contrast between the hypothesized cavity region and its surrounding area. The higher the contrast value is, the more likely the object state X corresponds to the cavity region in the input image. Therefore, the appearance model in (7) essentially relies on the relative contrast value among candidate object states rather than the absolute contrast value. As a consequence, this model has a merit of not being confounded by the interscan contrast variation (which in fact ranges remarkably from 0.07 to 0.37 for LV and 0.01 to 0.18 for RV in all the scans of our dataset). The mask $f^b(X)$ is formally

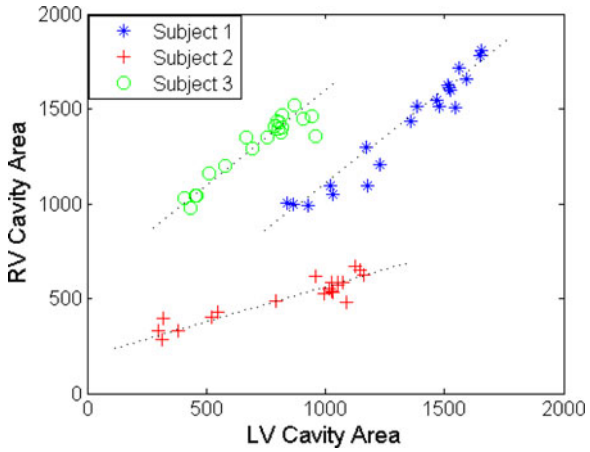

Fig. 8. Average linear correlation coefficient of 0.82 is obtained, between the manually segmented RV versus LV cavity areas from 56 subjects. Three subjects' RV cavity areas against LV cavity areas over a cardiac cycle are plotted in this figure, and the plots approximately lie on three straight lines.

Input: $\{s_i, 1/N\}_{i=1}^{N}$, $Z_{1:T}$
Output: $\mathcal{E}[A(X)|Z_t]$
1. Prepare the prior probability for both LV and RV.
For LV, $p_{LV}(X) = p_s(X)$ has been embedded in the sample set $\{s_i, 1/N\}_{i=1}^{N}$ as in Eq. (20).
For RV, compute the additional mutual information based prior term $f_{L\oplus R}(X, a, b, t)$ in Eq. (14).
2. Compute the likelihood function $p(Z_t|X = s_i)$ according to Eq. (6).
3. Compute the weight for each sample.
For LV, $\pi_i = p(Z_t|X = s_i)$.
For RV, $\pi_i = p(Z_t|X = s_i) \cdot f_{L\oplus R}(X, a, b, t)$.
4. Normalize $\{\pi_i\}_{i=1}^{N}$ to $\{\tilde{\pi}_i\}_{i=1}^{N}$.
5. Estimate the cavity area according to Eq. (19).

Fig. 9. Implementation of the adapted Bayesian formulation for area estimation using the *factored sampling* framework.

TABLE I
NUMBER OF THE SUBJECTS WITH LOWERED AND PRESERVED EFS FOR LV INDIVIDUALLY, RV INDIVIDUALLY, AND LV AND RV TOGETHER

	Lowered EF	Preserved EF
LV	24	32
RV	34	22
LV&RV	16	16

constructed as follows:

$$f_q^b(X) = \begin{cases} 1/A(X) & q \in \Omega_c(X) \\ -1/\{d \cdot \sum_{k\in\{1,\ldots,Q\}} (1 - \delta(\nabla X_k))\} & q \in \Omega_b(X) \\ 0 & \text{elsewhere,} \end{cases} \quad (8)$$

where d is the width of the band, $A(X)$ is the area of LV/RV, $\Omega_c(X)$ and $\Omega_b(X)$ are the cavity region and the surrounding narrow band determined by the object state X, and $\delta(\cdot)$ is the Dirac delta function.

2) Homogeneity Feature-Based Appearance Model: Filled with blood, the LV/RV cavity has a bright and homogeneous appearance in MRI except for the papillary muscle region. This observation provides a homogeneity constraint to the object state X, i.e., having low-intensity variance in its specified cavity region. In spite of the disturbance from the papillary muscles,

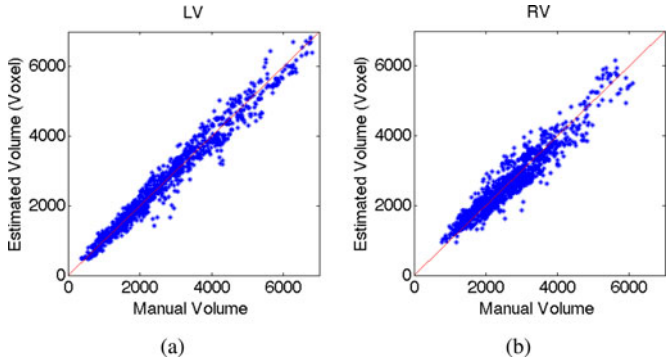

Fig. 10. Automatically estimated versus manually obtained volumes of (a) LV and (b) RV. The unit is voxel in 3-D image stack domain.

TABLE II
STATISTICAL APPRAISAL OF THE CONFORMITY BETWEEN THE AUTOMATICALLY ESTIMATED AND MANUALLY OBTAINED BIVENTRICULAR VOLUMES AND EFS

	$Corr(V_A,V_M)$	$Diff_V$	$Corr(EF_A,EF_M)$	$Diff_{EF}$
LV	0.985	0.073±0.064	0.966	0.037±0.032
RV	0.957	0.092±0.075	0.807	0.049±0.040

homogeneity can provide a complementary constraint along with others for such cavity estimation problems [17]. Therefore, we propose the following appearance model to capture the homogeneity feature:

$$p_h(Z|X) = 1 - \sum_{q\in\Omega_c(X)} (Z_q - \mu(Z,X))^2/A(X) \quad (9)$$

$$\mu(Z,X) = \sum_{q\in\Omega_c(X)} Z_q/A(X). \quad (10)$$

$\mu(Z,X)$ is the mean intensity within the cavity region $\Omega_c(X)$ specified by the object state X as the example mask shown in Fig. 7(b).

3) Edge Feature-Based Appearance Model: Edge features are frequently used especially in active contours-based segmentation [18] due to their popular existence and efficient computation. In this study, we employ edge features in both spatial and temporal domains. Edges in spatial domain correspond to high gradients along the boundaries between the cavity and myocardium. Edges in temporal domain correspond to the motion of the cavity boundary during diastolic and systolic periods. Accordingly, we define the edge-based appearance model as follows:

$$p_e(Z|X) = \langle Z^e, f^e(X)\rangle = \textstyle\sum_{q\in\{1,\ldots,Q\}} Z_q^e \cdot f_q^e(X) \quad (11)$$

where $f_e(X)$ is the edge mask [refer to the example in Fig. 7(c)] constructed based on X, and $f_q^e(X)$ is the qth pixel in the mask. The mask is formally constructed as

$$f_q^e(X) = \begin{cases} 1/\sum_{k\in\{1,\ldots,Q\}} (1 - \delta(\nabla X_k)) & q \in \Omega_e(X) \\ 0 & \text{elsewhere,} \end{cases} \quad (12)$$

where $\Omega_e(X)$ is the boundary of the cavity determined by the object state X. The edge image Z^e is given by $Z^e = \sqrt{(\partial_r Z)^2 + (\partial_c Z)^2} + |\partial_t Z|$, where $\partial_r Z$, $\partial_c Z$, and $\partial_t Z$ are the

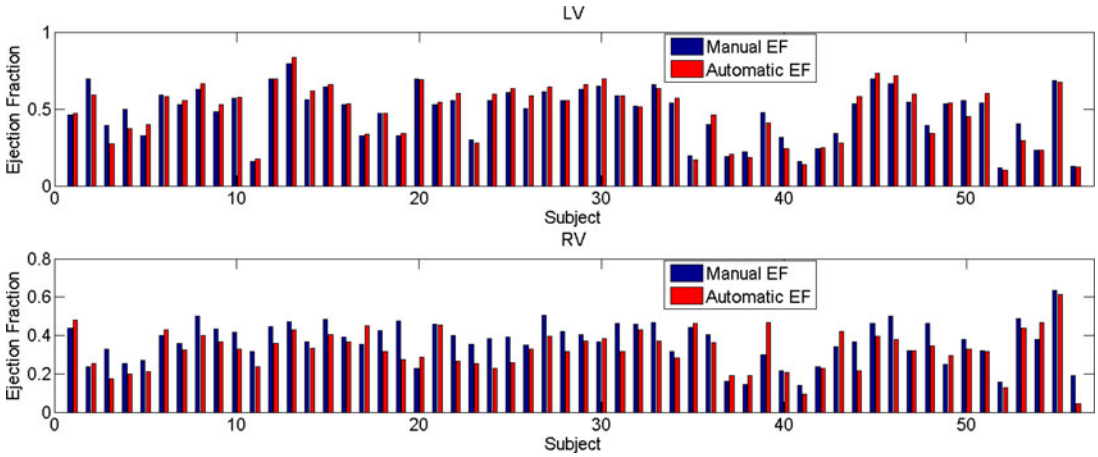

Fig. 11. Automatically estimated (red/right) versus manually obtained (blue/left) EFs of LV and RV. Data are sorted by the manually obtained EFs.

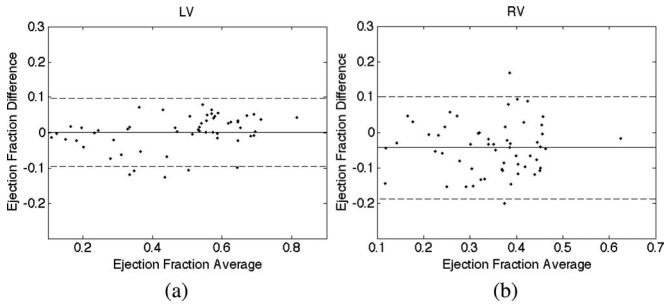

Fig. 12. Bland–Altman plots demonstrating the agreement between the EF values obtained based on the automatically estimated volumes and the manually obtained volumes for (a) LV and (b) RV. Mean difference and 95% limits of agreement are shown as solid and dotted lines, respectively.

first derivatives in the row, column, and temporal directions, respectively.

C. Proposed Prior Probability Model

In this paper, we propose a novel prior probability model to exploit the joint information between the two ventricles resulting from their motion similarity. As discussed in subsection III-A, LV and RV contract and expand following a similar pattern as shown in Fig. 2(b). This joint information can be expressed by a linear correlation between the volumes or the cavity areas of the two ventricles. We represent the joint information using area as

$$A_R(t) = a \cdot A_L(t) + b + \mathcal{N}(0, \sigma) \tag{13}$$

where $A_R(t)$ and $A_L(t)$ represent the cavity areas of RVs and LVs at a certain time $t \in \{1, \ldots, T\}$ during the cardiac cycle of T frames. $\mathcal{N}(0, \sigma)$ is a Gaussian noise. This correlation between the LV and RV cavity areas is confirmed by the manually segmented cavities in our dataset. An average linear correlation coefficient of 0.82 is obtained, between all the segmented RV and corresponding LV cavity areas from 56 subjects. The average residual and norm of residual for the linear regression fits for all subjects are 39.8787 (4.76% relative error) and 218.0085, respectively. Furthermore, the common measure for regression, R^2, is computed with an average result as 0.7775. All the numbers aforementioned indicate a good fit of the linear model in (13). To visually demonstrate the linear correlation between $A_R(t)$ and $A_L(t)$, Fig. 8 plots three randomly chosen subjects' RV versus LV cavity areas over their full cardiac cycles. As expected, the plots lie on three straight lines although with different values for a (slopes) and for b (RV-axis intercept). The slope a actually reflects the ratio between the diastolic/systolic degrees of LV and RV cavities, which varies from subject to subject. For example, a subject's LV contracts normally more than its RV in short-axis view, then the slope of this specific subject is usually smaller than one. To make the proposed method adaptive to this intersubject slope variations, the slope is automatically estimated for each individual subject in a way that will be described in the next paragraph.

Following (13), the estimated LV cavity areas over a cardiac cycle can be used to predict the RV cavity areas over the same cycle. With this prediction as a prior, more accurate RV posterior probability can be estimated than without such a prior. This prior is formulated and exploited by the correlation prior term $f_{L \oplus R}(X, a, b, t)$ within the following proposed prior probability model:

$$p_{\mathrm{RV}}(X) = p(X|a, b, t) = f_{L \oplus R}(X, a, b, t) \cdot p_s(X). \tag{14}$$

$p_s(X)$ is the underlying prior distribution embedded in the training set, and $f_{L \oplus R}(X, a, b, t)$ is derived following (13):

$$f_{L \oplus R}(X, a, b, t) = \frac{1}{\sqrt{2\pi}\sigma} \exp\left(-\frac{(aA_L(t) + b - A(X))^2}{2\sigma^2}\right). \tag{15}$$

The parameter t indicates the frame index of the current object state X during the cardiac cycle. Therefore, the current RV cavity area $A(X)$ [i.e., $A_R(t)$ in (13)] is linearly correlated to $A_L(t)$ (the LV cavity area in the same frame). The parameters a and b are estimated using maximum *a posteriori* estimation (MAP) method given all the images during the cardiac cycle,

$$[\hat{a}, \hat{b}]_{\mathrm{MAP}} = \arg\max_{[a,b]} p(a, b|Z_{1:T}) \tag{16}$$

TABLE III
IMPACT ANALYSIS OF EACH INDIVIDUAL COMPONENT IN THE PROPOSED METHOD, BLOB APPEARANCE MODEL (BLOB), EDGE APPEARANCE MODEL (EDGE), HOMOGENEITY APPEARANCE MODEL (HOMOGENEITY), AND PRIOR PROBABILITY MODEL (PRIOR)

		− Blob	− Edge	− Homogeneity	− Prior
RV	$Corr(EF_A,EF_M)$	0.415	0.636	0.712	0.759
	$Diff_{EF}$	0.084 ± 0.065	0.071±0.052	0.061±0.055	0.069±0.050
	$Corr(V_A,V_M)$	0.899	0.867	0.925	0.953
	$Diff_V$	0.146 ± 0.115	0.148±0.122	0.116 ± 0.122	0.094±0.075
LV	$Corr(EF_A,EF_M)$	0.891	0.966	0.845	-
	$Diff_{EF}$	0.058 ±0.051	0.037±0.032	0.070±0.059	-
	$Corr(V_A,V_M)$	0.979	0.985	0.977	-
	$Diff_V$	0.095 ± 0.097	0.073±0.064	0.101 ± 0.101	-

Each component is excluded from the proposed method in turn, and the corresponding results are reported in this table.

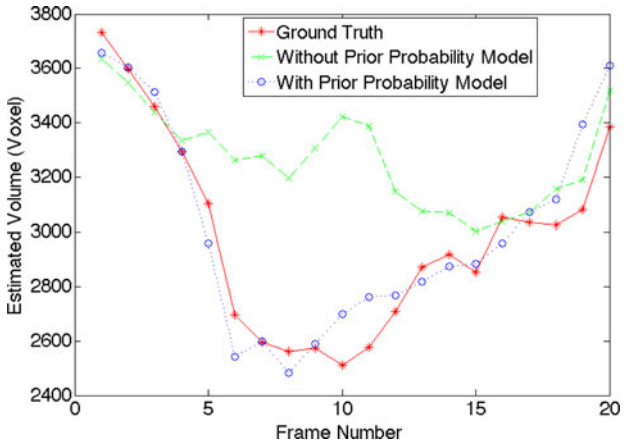

Fig. 13. Illustration of the prior probability model rectifying the portion of the volume curve with unexpected pattern.

where the posterior distribution $p(a,b|Z_{1:T})$ is computed as

$$\begin{aligned} p(a,b|Z_{1:T}) &= \sum_{X_1}\cdots\sum_{X_T} p(a,b,X_1,\ldots,X_T|Z_{1:T}) \\ &= \sum_{X_1}\cdots\sum_{X_T} p(Z_{1:T},X_1,\ldots,X_T,a,b)/p(Z_{1:T}) \\ &= \sum_{X_1}\cdots\sum_{X_T}\{p(Z_{1:T}|X_1,\ldots,X_T,a,b) \\ &\quad p(X_1,\ldots,X_T,a,b)\}/p(Z_{1:T}) \\ &= \sum_{X_1}\cdots\sum_{X_T}\{p(Z_1|X_1)\cdots p(Z_T|X_T) \\ &\quad p(X_1|a,b)\cdots p(X_T|a,b)p(a,b)\}/p(Z_{1:T}) \end{aligned} \tag{17}$$

In the previous equation, $p(a,b)$, the prior distribution of $[a,b]$, is assumed uniform, and $p(Z_{1:T})$ is a constant. $p(Z_t|X_t)$ and $p(X_t|a,b)=p(X|a,b,t)$ are defined in (6) and (14), respectively. A few assumptions are made in the derivation of (17), including the observation image at time t, Z_t, is independent to others given the object state at time t, X_t, and X_t is in turn assumed to be independent to others given the parameters a and b.

Notice that the prior probability model proposed in (14) is specifically designed for RV in order to exploit the corresponding LV area information. For the LV case, its prior probability model relies on the underlying prior distribution embedded in the training set,

$$p_{\text{LV}}(X) = p_s(X) \tag{18}$$

where $p_s(X)$ will be detailed in the following subsection.

D. Implementation

This subsection presents the implementation of the adapted Bayesian formulation proposed for cavity area estimation. The outline of the implementation is listed by the pseudocode in Fig. 9, and the details are introduced in the following.

Since the likelihood function $p(Z|X)$ in our adapted Bayesian estimation framework has a complex form, formulating the posterior probability $p(X|Z)$ in a closed form is not straightforward [19]. This problem is generally tackled in computer vision by iterative sampling techniques [20], among which the *factored sampling* algorithm [21] is widely accepted for the interpretation of static images [19]. This technique consists in generating a sample set $\{s_1,\ldots,s_N\}$ following a certain prior density $p(X)$ and then assigning to each sample s_i ($i\in\{1,\ldots,N\}$) a weight π_i based on the likelihood function as $\pi_i = p(Z|X=s_i)/\sum_{j=1}^{N} p(Z|X=s_j)$. The weighted sample set $\{s_i,\pi_i\}_{i=1}^{N}$ then serves as a representation of the posterior density $p(X|Z)$ whose accuracy increases as N increases. Consequently, the expectation of a function of the object state, e.g., the area function $A(X)$ in this paper $\mathcal{E}[A(X)|Z]$, can be generated directly from the sample set using the following approximation:

$$\mathcal{E}[A(X)|Z] \approx \sum_{i=1}^{N} A(s_i)\pi_i. \tag{19}$$

In this paper, instead of randomly generating the sample set $\{s_1,\ldots,s_N\}$, we obtain it directly from the training set. In the training phase, each of the input images is manually segmented into LV/RV and background. All the LV/RV binary segmentation images are collected together to build the sample set $\{s_1,\ldots,s_N\}$. This set naturally embeds various prior information about shape, location, and scale in the training set and approximates them as follows:

$$p_s(X) \approx \sum_{i=i}^{N} \delta(X,s_i)/N. \tag{20}$$

To incorporate additional prior other than $p_s(X)$ embedded in the training set, the sample weight is modified to involve not only likelihood but also prior terms. For example, the incorporation

TABLE IV
ROBUSTNESS ANALYSIS OF THE PROPOSED METHOD TO INTRA- AND INTERUSER VARIABILITY MEASURED BY ICCS

	ROI_center_x	ROI_center_y	ROI_orientation	ROI_scale	LV volume	LV EF	RV volume	RV EF
Intra-user	0.9962	0.9967	0.9838	0.9802	0.9961	0.9817	0.9828	0.8339
Inter-user	0.9950	0.9961	0.9641	0.9782	0.9929	0.9687	0.9680	0.8154

ROI related results (ROI_*) measure the consistency between two groups of ROIs selected by one user twice (Intrauser) or two separated users (Interuser). The left results measure the consistency between the automatically estimated cardiac parameters resulting from two different ROI groups.

TABLE V
IMPACT ANALYSIS OF WHETHER A SUBJECT'S EF IS LOWERED OR PRESERVED TO THE PERFORMANCE OF THE PROPOSED METHOD

	$Diff_{EF}$		P-value(t-test)
	Lowered EF	Preserved EF	
LV	0.035+0.036	0.038+0.030	0.8
RV	0.069+0.049	0.083+0.063	0.619

of the mutual information term $f_{L\oplus R}(X, a, b, t)$ proposed in (14) is achieved by computing the sample weight as the product of $f_{L\oplus R}(X, a, b, t)$ and the likelihood function $p(Z|X)$. Similarly, other types of correlation information between LV and RV could be exploited too.

The implementation discussed previously is formally described with the pseudocode in Fig. 9. The proposed method takes as input the initial evenly weighted sample set $\{s_i, 1/N\}_{i=1}^{N}$ and the MRI images over the cardiac cycle $Z_{1:T}$; and the output is the estimated cavity area at any time t within the cardiac cycle, $\mathcal{E}[A(X)|Z_t]$. In the following, we will explain the pseudocode in more details.

1) The first step prepares the prior probability for each sample s_i (refer to the pseudocode in Fig. 9).
2) The second step computes the likelihood for each sample s_i.
3) Given the prior probability and likelihood, the third step computes the weight π_i for each sample.
4) The fourth step performs normalization.
5) The fifth and last step estimates the cavity area based on the posterior probability approximated by the weighted sample set.

IV. EXPERIMENTS

In our experiments, a set of (3360 in total) two-dimensional (2-D) short-axis cine MR images from 56 clinical subjects (including both normal and abnormal cases as listed in Table I) were used. These images were acquired on a 1.5T scanner with fast-imaging employing steady-state acquisition image sequence mode, using these acquisition parameters: TR=2.98 ms, TE=1.2 ms, flip angle=30° , and slice thickness=10 mm. Each subject's data contain 20 frames throughout the cardiac cycle. In each frame, three representative slices, apical, mid-cavity, and basal, are selected following the standard AHA prescriptions [22] for validation, and their manual segmentations are used as the benchmark. In the following subsections, we will demonstrate the accuracy of the proposed method, conduct a thorough analysis of the method, and make comparisons with closely related works.

A. Accuracy Evaluation

In this subsection, we demonstrate the high accuracy of the proposed method in estimating the biventricular volumes of LV and RV using a *leave-one-out* strategy. Fig. 10 plots the estimated volumes (V_A) versus the ground truth (V_M) of LV and RV. The nearer the points to the identity line, the more accurate is the automatic estimation. In most of the cases, there is a very good conformity between the estimated volumes and the ground truth in both LV and RV cases. This is quantitatively justified by their calculated correlation coefficients [corr(V_A, V_M) in Table II] evaluated to 0.985 (LV) and 0.957 (RV). The relative error between the estimated volumes and the ground truth is also computed as $\mathrm{Diff}_V = \|V_A - V_M\|/V_M$ and reported in Table II. The very low relative error Diff_V (≤ 0.1) demonstrates the high accuracy of the automatically estimated volume compared to the ground truth.

Estimating the volumes of both LV and RV with such accuracy helps in assessing global cardiac functions. As an example, the EF that measures the blood volume pumped by a ventricle is used for the performance evaluation of the proposed method. The EF is computed using $(V_d - V_s)/V_d$, where V_d and V_s denote the largest (end-diastolic) and the smallest (end-systolic) volumes of a ventricle in a cardiac cycle. Fig. 11 illustrates a high conformity between the EF values obtained based on the automatically estimated volumes (EF_A) and the manually obtained volumes (EF_M). Similar information is also displayed using Bland–Altman plots in Fig. 12. This high conformity is further emphasized with the correlation coefficients and the proposed method yielded the coefficients 0.966 and 0.807, respectively, for the LV and RV cases. In addition, we report the mean and standard deviation of the errors between the automatic and the manual EFs given by $\mathrm{Diff}_{\mathrm{EF}} = \|\mathrm{EF}_A - \mathrm{EF}_M\|$ in Table II. The very low mean (≤ 0.05) and standard deviation (≤ 0.05) of $\mathrm{Diff}_{\mathrm{EF}}$ confirm the high consistency between the manual and automatic EFs. By analyzing all the results discussed previously, it can be observed that LV has relatively more accurate results than RV. It is consistent with the literature that RV is still a completely unsolved problem [2]. The difficulty in RV estimation includes: complex geometry, disturbing surrounding structure, and trabeculation. These are the potential focuses that require further study in order to improve the RV accuracy.

B. Method Analysis

In this subsection, we investigate three aspects of the proposed method. The first one is the impact of each proposed component in the adapted Bayesian formulation. These components include the blob appearance model, edge appearance model, homogeneity appearance model, and prior probability model. The second one is the robustness of the proposed method to intra- and interuser variability in terms of ROI selection. The last one is the

TABLE VI
COMPARISON BETWEEN THE PROPOSED METHOD AND THE RECENTLY PUBLISHED COMPETING METHODS: THE NEURAL NETWORK-BASED REGRESSION METHOD IN [11], GRAPH-CUT-BASED SEGMENTATION METHOD IN [6], AND LEVEL-SET-BASED SEGMENTATION METHOD IN [24]

Method	LV/RV	Subjects nb.	*mean*($Diff_{EF}$)	*std*($Diff_{EF}$)	$CPU(s)$
The proposed method	LV&RV	56	0.037	0.032	0.49
Neural network regression	LV	20	0.016	0.016	0.21
Graph-cut segmentation	LV	20	0.097	0.092	9.62
Level-set segmentation	LV	20	0.110	0.125	494.45

LV/RV indicates whether the method applies to LV or RV.

impact of whether a testing subject has a lowered or preserved EF to the performance of the proposed method.

Table III reports the performance of the proposed method when each of its proposed components is excluded in turn. Compared to the results in Table II where no component is excluded, the performance degrades in all the cases, which indicates that each component is indispensable and contributes with the others in a complementary way. In terms of the three appearance models within the likelihood function, the blob and edge appearance models generally impact the method more than the homogeneity appearance model whose performance degrades the least. As far as the prior probability model is concerned, it affects the performance relatively less than the appearance models. It is because in most of the images, using the appearance models alone has already resulted in accurate estimation. Even in a failure case as shown in Fig. 13, the estimated volumes in the two ends of the cardiac cycle still match the ground truth properly without using the prior probability model. Only when the appearance models fail totally as the middle cycle portion, the prior probability model will contribute and rectify this error using its imposed constraint. This improvement as confirmed in Table III is crucial to the EF estimation, because the EF is affected only by the volumes at the two times: end-systole and end-diastole, whose small errors can result in big errors of EF. In fact, with LV providing a prior to RV, the correlation coefficient between RV's automatic and manual EFs increases from 0.759 to 0.807, and the mean error between RV's automatic and manual EFs decreases from 0.069 to 0.049.

The second aspect investigated is the robustness of the proposed method to the intra- and interuser variability in terms of ROI selection. Due to the distinct landmarks used in our ROI extraction step, the proposed method can robustly estimate the cardiac parameters allowing the existence of intra- and interuser variability. To demonstrate it, two users independently select the ROIs according to the description in subsection II-A, and one of them selects the ROIs for the second time after an interval of ≥ 15 days. The intraclass correlation coefficient (ICC) [23] is employed to evaluate the resemblance between two groups of ROIs and their corresponding estimated cardiac parameters. Table IV reports the corresponding ICC results computed from the extracted ROIs' specifications (including center, orientation, and scale) and the estimated functional parameters of the two ventricles. The high values related to ROIs' specifications indicate that the proposed way of ROI extraction generates highly consistent ROIs due to the distinct landmarks used. Consequently, the final estimation results of cardiac functional parameters are highly robust to the intra- and interuser variability as illustrated in Table IV.

The third analysis investigates if the proposed method is affected by whether a testing subject has a lowered or preserved EF. This analysis compares the estimated EF results from the two groups (subjects with lowered manual EFs and subjects with preserved manual EFs). Table V reports the mean and standard deviation of the errors between automatic and manual EFs from the two groups, respectively. As shown in the table, whether a subject has a lowered or preserved EF does not make a statistically significant difference between the results of the two groups according to a parametric test (two-tailed *t*-test). Therefore, the proposed method is suitable for processing both subjects with preserved EFs and subjects with lowered EFs.

C. Comparison

Although there is no existing method that estimates the left and right ventricular volumes jointly and without segmentation, we include a comparison analysis for integrity. Table VI shows a comparison on LV between our method and related methods reported in the thesis version [12] of the closest work to ours [11].

In this comparison, accuracy is measured by the mean error and standard deviation of EF, and efficiency is measured by the computational time. As shown in Table VI, the proposed method obviously outperforms segmentation-based methods represented by the recent works using graph-cut [6] and level-set [24] in both accuracy and efficiency. Compared to the neural network-based (NNB) regression method, our method and results have three superiorities even though its performance on LV is slightly lower: 1) our method applies to both LV and RV jointly while the NNB method does not apply to RV directly as analyzed in the introduction; 2) our method is robust to both intra- and interuser variability while the NNB method is very sensitive to its user inputs as analyzed in [12]; 3) our results are obtained from 56 subjects which is more than twice the size of the dataset (20 subjects) where the NNB results are obtained.

V. CONCLUSION

This paper proposed a real-time *segmentation-free* method that is able to estimate the biventricular volumes jointly. The experimental results obtained on 56 subjects showed that the method produced highly consistent results with human expert. Furthermore, the idea of estimating the object area with the Bayesian framework and the proposed multifeature likelihood function can be potentially generalized and applied to a multitude of similar applications. Our future work includes: extending the method to be fully automatic by removing the user

intervention, and applying the proposed method to other modalities and problems as a general area/volume estimation approach.

REFERENCES

[1] D. Lloyd-Jones, R. J. Adams, T. M. Brown, M. Carnethon, S. Dai, G. De Simone, T. B. Ferguson, E. Ford, K. Furie, C. Gillespie, A. Go, K. Greenlund, N. Haase, S. Hailpern, P. M. Ho, V. Howard, B. Kissela, S. Kittner, D. Lackland, L. Lisabeth, A. Marelli, M. M. McDermott, J. Meigs, D. Mozaffarian, M. Mussolino, G. Nichol, V. L. Roger, W. Rosamond, R. Sacco, P. Sorlie, R. Stafford, T. Thom, S. Wasserthiel-Smoller, N. D. Wong, and J. Wylie-Rosett, "Heart disease and stroke statistics–2010 update: A report from the American heart association," *Circulation*, vol. 121, no. 7, pp. e46–e215, Feb. 2010.

[2] C. Petitjean and J.-N. Dacher, "A review of segmentation methods in short axis cardiac MR images," *Med. Image Anal.*, vol. 15, no. 2, pp. 169–184, Apr. 2011.

[3] H.-y. Lee, N. C. F. Codella, M. D. Cham, J. W. Weinsaft, and Y. Wang, "Automatic left ventricle segmentation using iterative thresholding and an active contour model with adaptation on short-axis cardiac MRI," *IEEE Trans. Biomed. Eng.*, vol. 57, no. 4, pp. 905–913, Apr. 2010.

[4] M. Lynch, O. Ghita, and P. F. Whelan, "Automatic segmentation of the left ventricle cavity and myocardium in MRI data," *Comput. Biol. Med.*, vol. 36, no. 4, pp. 389–407, Apr. 2006.

[5] C. a. Cocosco, W. J. Niessen, T. Netsch, E.-J. P. a. Vonken, G. Lund, A. Stork, and M. a. Viergever, "Automatic image-driven segmentation of the ventricles in cardiac cine MRI," *J. Magn. Reson. Imag.*, vol. 28, no. 2, pp. 366–374, Aug. 2008.

[6] I. B. Ayed, K. Punithakumar, S. Li, A. Islam, and J. Chong, "Left ventricle segmentation via graph cut distribution matching," *Int. Conf. Med. Image Comput. Comput.-Assisted Intervention*, pp. 901–909, Jan. 2009.

[7] I. Ben Ayed, A. Mitiche, M. B. Salah, and S. Li, "Finding image distributions on active curves," *Comput. Vis. Pattern. Recog.*, vol. 1, pp. 3225–3232, Jun. 2010.

[8] X. Zhuang, D. J. Hawkes, W. R. Crum, R. Boubertakh, S. Uribe, D. Atkinson, P. Batchelor, T. Schaeffter, R. Razavi, and D. L. G. Hill, "Robust registration between cardiac MRI images and atlas for segmentation propagation," in *Proc. Soc. Photo-Opt. Instrum. Eng. Conf.*, Mar. 2008, p. 691408.

[9] A. Andreopoulos and J. K. Tsotsos, "Efficient and generalizable statistical models of shape and appearance for analysis of cardiac MRI," *Med. Image Anal.*, vol. 12, no. 3, pp. 335–357, Jun. 2008.

[10] J. Senegas, C. A. Cocosco, and T. Netsch, "Model-based segmentation of cardiac MRI cine sequences a Bayesian formulation," *Proc. SPIE, Med. Imag.*, vol. 5370, pp. 432–443, May 2004.

[11] M. Afshin, I. B. Ayed, A. Islam, A. Goela, T. M. Peters, and S. Li, "Global assessment of cardiac function using image statistics in MRI," *Int. Conf. Med. Image Comput. Comput.-Assisted Intervention*, pp. 535–543, Jan. 2012.

[12] M. Afshin, "Automatic assessment of cardiac left ventricular function via magnetic resonance images," Ph.D. dissertation, Univ. of Western Ontario, London, ON, Canada, 2012.

[13] Z. Wang, M. B. Salah, I. B. Ayed, A. Islam, A. Goela, and S. Li, "Biventricular volume estimation for cardiac functional assessment," presented at the Radiol. Soc. North Amer., Chicago, IL, USA, 2013.

[14] T. Kukulski, L. Hfibbert, M. Arnold, and B. Wranne, "Normal regional right ventricular function and its change with age: A Doppler myocardial imaging study," *J. Amer. Soc. Echocardiogr.*, vol. 13, pp. 194–2004, 2000.

[15] D. Serby, E. Meier, and L. Van Gool, "Probabilistic object tracking using multiple features," in *Proc. 17th Int. Conf. Pattern Recogn.*, 2004, vol. 2, pp. 184–187.

[16] T. Lindeberg, *Scale-Space Theory in Computer Vision*. New York, NY, USA: Springer-Verlag, 1994, pp. 249–271.

[17] M. Jolly, "Fully automatic left ventricle segmentation in cardiac cine MR images using registration and minimum surfaces," in *Proc. Worksh. Cardiac Magn. Reson. Left Ventricle Segment.*, 2009.

[18] M. Kass, A. Witkin, and D. Terzopoulos, "Snakes: Active contour models," *Int. J. Comput. Vis.*, vol. 1, no. 4, pp. 321–331, 1988.

[19] A. Blake and B. Bascle, "Statistical models of visual shape and motion," *Philos. Trans. Roy. Soc. London A*, vol. 356, pp. 1283–1302, 1998.

[20] G. Storvik, "A Bayesian approach to dynamic contours through stochastic sampling and simulated annealing," *IEEE Trans. Pattern Anal. Mach. Intell.*, vol. 16, no. 10, pp. 976–986, Oct. 1994.

[21] U. Grenander, Y.-s. Chow, and D. M. Keenan, *A Pattern Theoretical Study of Biological Shapes*. New York, NY, USA: Springer-Verlag, 1991.

[22] M. S. V. M. D. Cerqueira, N. J. Weissman, V. Dilsizian, A. K. Jacobs, S. Kaul, W. K. Laskey, D. J. Pennell, J. A. Rumberger, and T. Ryan, "Standardized myocardial segmentation and nomenclature for tomographic imaging of the heart: A statement for healthcare professionals from the cardiac imaging committee of the council on clinical cardiology of the American heart association," *Circulation*, vol. 105, no. 4, pp. 539–542, Jan. 2002.

[23] G. G. Koch, "Intraclass correlation coefficient," in *Encyclopedia of Statistical Science*, 4th ed. New York, NY, USA: Wiley, 1982, pp. 213–217.

[24] I. Ben Ayed, S. Li, and I. Ross, "Embedding overlap priors in variational left ventricle tracking," *IEEE Trans. Med. Imag.*, vol. 28, no. 12, pp. 1902–1913, Dec. 2009.

Authors' photographs and biographies not available at the time of publication.